crystal vibrations by considering a single unit cell of the crystal.

The classification of the electronic states, in terms of the factor (space) group of the crystal, can also be found by the correlation of Bhagavantan and Venkatarayudu methods.[44] Since the electronic functions can be represented as simple products of single ion electronic states and we are only interested in single excitations, there will be a one-pair function for the unexcited ground state and eight singly excited pair functions. The correlation between the free CuF$_6^{4-}$ ion and the site and factor group symmetries is shown in Figure 18. The four transitions for the free molecule in this orbital basis increases to eight for the two molecules per unit cell.

Contribution from the Department of Chemistry, Stanford University, Stanford, California 94305,
and Laboratoire d'Optique Physique, ESPCI, 10 rue Vauquelin, 75231 Paris Cedex 05, France

Variable-Photon-Energy Photoelectron Spectroscopic Studies of High-Spin d^6 Tetrahedral FeCl$_4^{2-}$: Electronic Relaxation Effects on Ionization

Kristine D. Butcher,† Stephen V. Didziulis,† Bernard Briat,‡ and Edward I. Solomon*,†

Received September 20, 1989

Variable-photon-energy photoelectron spectra (PES) are reported for the valence band region of ferrous chloride over the energy range 25–150 eV. Changes in peak intensity as a function of photon energy are compared to atomic photoionization cross sections, allowing experimental assignment and quantitation of the PES features. These results indicate that the ground-state-bonding description in ferrous chloride corresponds to the normal description for transition-metal complexes, with the highest occupied levels containing mostly metal character, but with significant spin-polarization effects. The relatively large exchange splitting in d^6 splits the d levels into spin-up and spin-down sets, with the majority spin-up levels showing greater covalent mixing in both the experimental data and in spin-unrestricted SCF–Xα–SW calculations. The PE spectra further show satellite peaks with significant off-resonance intensity ($\sim$6% of the main-band intensity), indicating that a large electronic relaxation occurs upon ionization. PE spectra taken at the Fe 3p absorption edge show dominant resonance enhancement in the deeper binding-energy region of the main band as well as in the satellites. The Xα–SW calculations reproduce both the large relaxation effects and the observed resonance behavior and assign the satellites as arising from ligand ionization plus ligand-to-metal charge-transfer shakeup. The resonance profiles of ferrous chloride are very similar to those of ferric chloride, which shows no relaxation on ionization, but has an inverted energy level description for the majority spin-up levels in the ground state (with the highest occupied orbital containing mostly ligand character). The resonance PES profiles thus indicate that ionized ferrous chloride has relaxed sufficiently to become inverted due to the decrease in electron repulsion and increase in exchange stabilization present in the high-spin d^5 final state. The role of exchange in determining both the ground-state bonding and its change on ionization are considered, and the implications of electronic relaxation for ferrous redox chemistry are discussed.

I. Introduction

High-spin ferrous complexes play an important role in inorganic redox chemistry, particularly in bioinorganic systems. The single iron–sulfur site in rubredoxin has been the focus of a number of theoretical and spectroscopic studies.[1,2] For the ferrous state, a normal ground-state-bonding description is predicted with the antibonding HOMO containing mostly metal character.[1a] However, calculations on high-spin ferric systems indicate the presence of an inverted ground-state-bonding scheme with the HOMO described as mostly ligand in character.[1c] This inverted ground state has now been demonstrated experimentally in our photoelectron spectroscopic (PES) studies of FeCl$_4^-$, and is due to the large exchange stabilization of the high-spin d^5 configuration.[3] Spin-unrestricted (but not spin-restricted) SCF–Xα scattered-wave calculations reproduce our experimental PES data and show that the majority spin (spin-up, ↑) energy levels (i.e. those having the same spin as the uncompensated valence electrons) are energetically stabilized and have significantly different wave functions relative to their spin-down (↓) counterparts. In addition, both the PES data and the Xα calculations show that the ferric system exhibits little change in electronic structure, (i.e. orbital relaxation) upon ionization. These results indicate that a large change in the iron electronic structure occurs upon oxidation. The goal of this study is to use PES to experimentally determine the bonding scheme present in the ferrous tetrachloride ground state and its change upon ionization and to relate this to electronic relaxation contributions to redox processes.[4]

Our previous PES study of d^9 CuCl$_4^{2-}$ systems demonstrated that dramatic wave function changes can occur upon ionization.[4a] The orbitals relax in order to minimize the large change in metal-centered electron repulsion that can occur upon ionization. As a result of this relaxation, intensity is shifted from the main-band, one-electron PES peaks into deeper binding-energy satellite peaks.[5] The satellite peak corresponds to the simultaneous ionization plus shakeup of a second electron to create an excited final state of the complex (Scheme I). This formally two-electron transition is forbidden and should have no intensity. However, final-state relaxation allows the wave functions to change and thus intensity is shifted from the lowest energy final state into the excited (satellite) final state, provided that the shakeup involves an energy level of the same symmetry as the one-electron-ionized final state.[6]

Scheme I

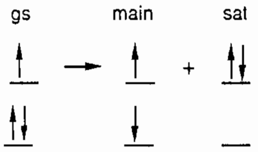

In order to make a detailed assignment and quantitative evaluation of the valence band PES features, we exploit the changes in peak intensity with input photon energy using syn-

---

† Stanford University.
‡ ESPCI.

(1) (a) Bair, R. A.; Goddard, W. A., III. *J. Am. Chem. Soc.* **1978**, *100*, 5669. (b) Norman, J. G., Jr.; Ryan, P. B.; Noodleman, L. *J. Am. Chem. Soc.* **1980**, *102*, 4279. (c) Norman, J. G., Jr.; Jackels, S. C. *J. Am. Chem. Soc.* **1975**, *97*, 3833.

(2) (a) Deaton, J. C.; Gebhard, M. S.; Koch, S. A.; Millar, M.; Solomon, E. I. *J. Am. Chem. Soc.* **1988**, *110*, 6241. (b) Deaton, J. C.; Gebhard, M. S.; Solomon, E. I. *Inorg. Chem.* **1989**, *28*, 877. (c) Gebhard, M. S.; Deaton, J. C.; Koch, S. A.; Millar, M.; Solomon, E. I. *J. Am. Chem. Soc.*, in press.

(3) Butcher, K. D.; Didziulis, S. V.; Briat, B.; Solomon, E. I. *J. Am. Chem. Soc.*, in press.

(4) (a) Didziulis, S. V.; Cohen, S. L.; Gewirth, A. A.; Solomon, E. I. *J. Am. Chem. Soc.* **1988**, *110*, 250. (b) Didziulis, S. V.; Cohen, S. L.; Butcher, K. D.; Solomon, E. I. *Inorg. Chem.* **1988**, *27*, 2238.

(5) (a) Frost, D. C.; Ishitani, A.; McDowell, C. A. *Mol. Phys.* **1972**, *24*, 861. (b) van der Laan, G. *Solid State Commun.* **1982**, *42*, 165. (c) Thuler, M. R.; Benbow, R. L.; Hurych, Z. *Phys. Rev. B: Condens. Matter* **1982**, *26*, 669.

(6) Manne, R.; ÅAberg, T. *Chem. Phys. Lett.* **1970**, *7*, 282.

0020-1669/90/1329-1626$02.50/0

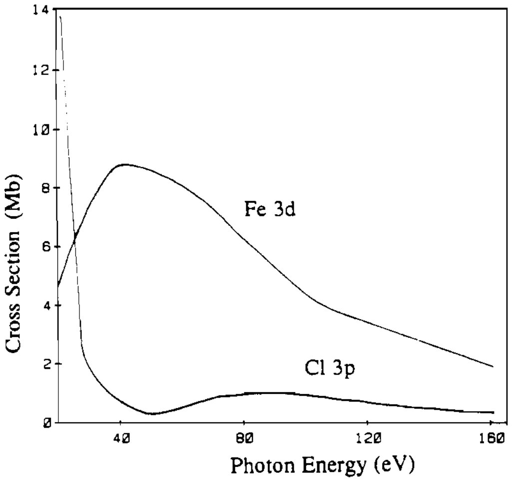

Figure 1. Photon-energy dependence of the atomic photoionization cross section (adapted from ref 7a).

chrotron radiation. The aspects of the photoionization cross section, σ, of interest are (1) the general changes in σ with input photon energy and (2) resonance effects, which involve initial excitation to bound states. The Fe 3d and Cl 3p cross sections[7a] are plotted in Figure 1. In general, metal 3d cross sections show a broad, delayed intensity maximum peaking in the photon-energy region 40–50 eV, while the Cl 3p cross section peaks near threshold and then decreases with increasing photon energy.[7] The Cl 3p σ also exhibits a local intensity minimum near 50 eV due to the node in the radial wave function.[8] While the cross section behavior of a PES feature is a function of both the initial and final state wave functions, the experimental main-band peak intensity changes with photon energy have been found to reflect the *initial*-state bonding description, even in the presence of extensive orbital relaxation.[4a] Thus, the main-band intensity changes observed in the PES spectra may be used to probe the initial-state covalency, without significant complications from final-state relaxation.

Resonance effects that occur near the metal 3p absorption edge can substantially change the photoionization cross section and provide a sensitive probe of the final-state character in the PES peaks. The resonance process, defined by Davis,[9] is outlined in Scheme II.

Scheme II

$$\text{d ionization} \quad \text{Fe } 3p^6 3d^6 \rightarrow 3p^6 3d^5$$

$$\text{resonance} \quad \text{Fe } 3p^6 3d^6 \rightarrow 3p^5 3d^7 \rightarrow 3p^6 3d^5$$

At the absorption edge, a metal 3p electron is excited to the metal 3d level. This excited state autoionizes through a super-Coster–Kronig (SCK) Auger decay process, resulting in a $|d^5\rangle$ final state, which is the same state reached by direct d ionization. The localized nature and large repulsion of the d electrons gives the autoionization process responsible for the resonance intensity a high probability. Because the resonance process specifically enhances the $|d^5\rangle$ final state, the presence of resonance intensity in PES features at the Fe 3p edge serves to define the metal distribution in the final states.

In section III, we present the variable energy photoelectron spectral results for the valence band region of FeCl$_4^{2-}$. In section IVA, the cross section dependence on the input photon energy will be used to assign the PES valence band features, and the results correlated to ground- (initial-) state spin-unrestricted SCF-Xα–SW calculations. In section IV.B, the additional effects of final-state relaxation are considered by comparison to one-electron-ionized and transition-state Xα–SW results. An assignment of the satellites is made, and the extent of relaxation upon valence ionization is probed. In section IV.C, the resonance PES results are analyzed on the basis of the model of Davis.[9a] The reliability of the Xα–SW calculations is assessed by using the Xα wave functions to generate theoretical resonance spectra for comparison to experiment. From these studies, it is determined that the ground state present in ferrous tetrachloride has antibonding levels that contain mostly metal character and that electronic relaxation drastically changes the wave functions on ionization to produce highest occupied antibonding levels with mostly ligand character. The role of exchange in determining both the ground-state-bonding description and its change on ionization are considered, and the implications of electronic relaxation for ferrous redox chemistry are discussed.

II. Experimental Section

The tetragonal Cs$_3$FeCl$_5$ and Rb$_3$FeCl$_5$ single crystals used in this study are isomorphous, with space group $I4/mcm$ and D_{2d}-distorted tetrahedral Fe site symmetry.[10,11] The crystals were mounted on an Al stub with UHV compatible Torrseal (Varian Associates) and cleaned in a nitrogen atmosphere by polishing with 9-μm grit Al$_2$O$_3$ plastic lapping sheet. After transfer to UHV under N$_2$, further cleaning was performed by grinding with 100-μm grit diamond particles embedded in a nickel wheel. Cleanliness was checked by the presence of satisfactory valence band spectra at low photon energies where the cross sections for valence levels of common contaminants are high. In addition, sample purity was checked by using core-level XPS (O 1s, C 1s) prior to use at the Stanford Synchrotron Radiation Laboratory (SSRL).

All XPS data were obtained on a Vacuum Generators (VG) ESCALAB Mk II. instrument. The ESCALAB instrument contains a twin-anode X-ray source (Mg Kα, 1253.6 eV, and Al Kα, 1486.6 eV), which was operated at $<$90 W to minimize damage. Samples were cooled to 160 K, and the pass energy was maintained at 20 eV. All ESCALAB spectra were obtained at normal emission. Details of the ESCALAB system have been described elsewhere.[4] The PES data were obtained by using a Perkin-Elmer PHI system, employing synchrotron radiation at SSRL on SPEAR beam line III-1, which is equipped with a Grasshopper monochromator.[12] The PHI system operated at a base pressure of $<1 \times 10^{-10}$ Torr, and has been described elsewhere.[4] Variable inlet and exit slits on the monochromator allowed a constant energy resolution of 200 meV to be maintained, and beam-line transmission filters were used up to 70 eV to minimize higher order light contributions to the monochromatic radiation.[12c] The pass energy for all synchrotron PES spectra was maintained at 25 eV. Constant-initial-state (CIS) spectra were obtained by simultaneously scanning the photon energy and analyzed kinetic energy such that the intensity profile of a peak at constant binding energy is generated. The slit widths were adjusted such that the photon energy resolution was always better than 200 meV, and the pass energy was increased to 50 eV to allow greater signal intensity. Constant-final-state (CFS) spectra, which are equivalent to absorption edges,[13] were obtained by using partial yield detection by scanning the photon energy while analyzing 8.0-eV kinetic energy electrons in the secondary tail. The slits and pass energy were set as with CIS.

An electron flood gun was required to neutralize surface charging during data collection at SSRL due to the insulating properties of the material. Gun operating conditions of 10–100 nA at 0.5–1.5 V were sufficient for obtaining spectra. All spectra were signal averaged, with 40–60 scans necessary for satisfactory signal to noise. Scans were collected in sets of 10 each, which were added together after compensating for any kinetic energy shifts. All data taken at SSRL (PES, CIS, CFS) were normalized to the incident photon flux by a flux monitor, which consists of a sodium salicylate coated stainless-steel or nickel mesh located

---

(7) (a) Yeh, J. J.; Lindau, I. *At. Data Nucl. Data Tables* **1985**, *32*, 1. (b) Fano, U.; Cooper, J. W. *Rev. Mod. Phys.* **1968**, *40*, 441. (c) Manson, S. T.; Cooper, J. W. *Phys. Rev.* **1968**, *165*, 126. (d) Eastman, D. E.; Kusnietz, M. *J. Appl. Phys.* **1971**, *42*, 1396. Note: The photoionization cross sections tabulated by Yeh are for atomic species. In order to approximate the effect of the positive charge on the Fe^{2+} ion, the Ni 3d cross sections were used for calculations in this paper.

(8) Cooper, J. W. *Phys. Rev.* **1962**, *128*, 681.

(9) (a) Davis, L. C. *Phys. Rev. B: Condens. Matter* **1982**, *25*, 2912. (b) Davis, L. C.; Feldkamp, L. A. *Phys. Rev. B: Condens. Matter* **1981**, *23*, 6239.

(10) (a) Briat, B.; Canit, J. C. *Mol. Phys.* **1983**, *48*, 33. (b) Seifert, H.-J.; Klatyk, K. *Z. Anorg. Allg. Chem.* **1966**, *342*, 1.

(11) (a) Powell, H. M.; Well, A. M. *J. Chem. Soc.* **1935**, 359. (b) Figgis, B. N.; Gerloch, M.; Mason, R. *Acta Crystallogr.* **1964**, *17*, 506.

(12) (a) Brown, F. C.; Bachrach, R. Z.; Lien, N. *Nucl. Instrum. Methods* **1978**, *152*, 73. (b) Stohr, J. *Instruction Manual for the New Grasshopper Monochromator*; Stanford Synchrotron Radiation Laboratory: Stanford, CA, 1980. (c) Pate, B. B. Ph.D. Thesis, Stanford University, 1984.

(13) (a) Stohr, J.; Jaeger, R.; Brennan, S. *Surf. Sci.* **1982**, *117*, 503. (b) Hecht, M. Ph.D. Thesis, Stanford University, 1982.

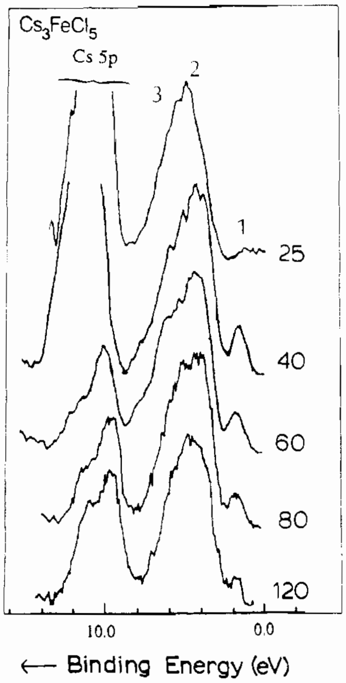

Figure 2. Variable-photon-energy valence band PES data for Cs_3FeCl_5. All spectra are normalized to peak 2.

in the path of the incident radiation and a total yield channeltron detector.

Standard versions of the Xα–SW code were used to calculate the molecular orbital energy levels and wave functions of the $FeCl_4^{2-}$ cluster. The α values of Schwarz[14] and l values up to 4, 3, and 2 were used for the outer, iron, and chloride spheres, respectively. A tetrahedral geometry was employed, with an average Fe–Cl bond length of 2.29 Å.[10,15] The optimum overlapping sphere radii were determined by fitting the transition-state energy of the $^5E \rightarrow {}^5T_2$ d–d band to the experimental value[16] of 4000 cm^{-1} while maintaining matching potentials at the sphere boundaries. As a secondary check, the $1t_1\downarrow \rightarrow 2e\downarrow\ {}^5T_2$ charge-transfer transition-state energy was calculated and compared to an experimental estimate.[17] The d–d transition energy for each set of trial radii was determined by using the Slater transition state method by transferring 0.5 electron from the $2e\downarrow$ level to the $5t_2\downarrow$ level, and reconverging the potential. The charge-transfer-transition energy was determined in the same manner. The final sphere radii for Fe and Cl were 3.00 and 2.50 bohr, respectively.

III. Results

PE spectra for Cs_3FeCl_5 and Rb_3FeCl_5 were obtained over the energy range 25–120 eV. Selected spectra for Cs_3FeCl_5 are given in Figure 2, normalized to the highest peak. The spectra exhibit five peaks between 2 and 12 eV binding energy, with all binding energies referenced to the Cl $2p_{3/2}$ level at 198.7 eV.[4b] The two peaks at 10.0 and 11.8 eV have been assigned as the spin–orbit split Cs $5p_{3/2,1/2}$ in accordance with previous work on $CsFeCl_4$ and CsCl.[3,4a] The remaining peaks in the main band are therefore due to $FeCl_4^{2-}$ photoemission, and are labeled as peaks 1–3 in Figure 2. (Note that the peak 2–3 region is rather broad, with peak 2 referring to the low-energy part of the band and peak 3 to the deeper energy side. The clearest definition of the two regions is present in the 60-eV spectrum of Figure 2.) Several changes in the relative intensities of these features occur as the input photon energy is increased from 25 to 40 eV. Peak 1 shows an increase in intensity relative to peaks 2 and 3, reaching a maximum at ~40 eV. Also, peak 3 shows a slight decrease in intensity relative to peak 2, and the peak 2–3 band region becomes more asymmetric with the center shifting to lower binding energy. Based on the theoretical photoionization cross section behavior outlined in the introduction, these results indicate that peak 1 contains dominantly Fe 3d character, while peak 2 and peak 3 contain more Cl 3p character with peak 3 containing the most Cl 3p character. While the data in Figure 2 give only relative intensity information, the absolute peak intensity profiles for these data were obtained from a three-peak Gaussian/Lorentzian fit[18] and are plotted in Figure 3. The integrated absolute intensity of peak 1 (insert) shows a maximum at 40 eV, confirming its assignment as an antibonding ionization having dominant Fe 3d character. However, both peak 2 and peak 3 show absolute intensity profiles characteristic of Cl 3p. The peak intensity change for peak 2 relative to peak 3, obtained by dividing one peak area by the other, shows an increase with increasing photon energy up to 50 eV. This indicates greater relative Fe 3d character is present in peak 2, consistent with the qualitative observations from the PES data in Figure 2. Since it is unreasonable to assign peak 1 as containing all six antibonding

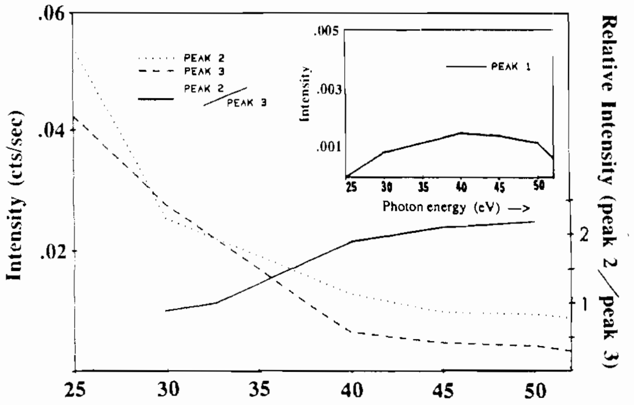

Figure 3. Absolute and relative intensity profiles of the $FeCl_4^{2-}$ features through the Cl 3p Cooper minimum (Scale at left for peak 2 (···) and peak 3 (- - -), scale at right for peak 2/peak 3 ratio (—)). The inset gives peak 1 intensity at higher sensitivity.

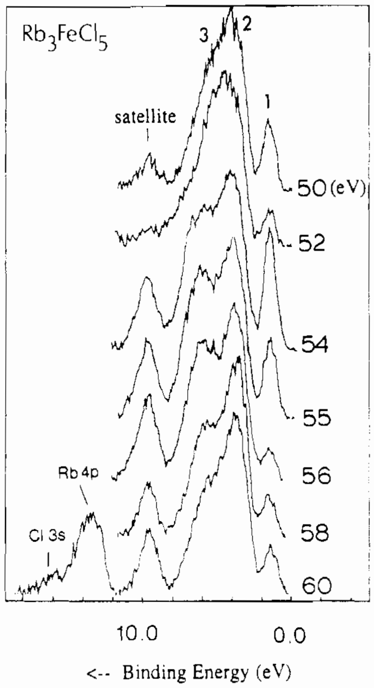

Figure 4. Resonance PES data for Rb_3FeCl_5 at the Fe 3p absorption edge.

---

(14) Schwarz, K. *Phys. Rev. B: Condens. Matter* **1972**, *5*, 2266.

(15) Lauher, J. W.; Ibers, J. A. *Inorg. Chem.* **1975**, *14*, 348.

(16) Furlani, C.; Cervone, E.; Valenti, V. *J. Inorg. Nucl. Chem.* **1963**, *25*, 159.

(17) Day, P.; Jørgenson, C. K. *J. Chem. Soc.* **1964**, 6226.

(18) This iterative peak fitting procedure allows the independent variation of peak position, Lorentzian peak width, and peak height to minimize the χ^2 difference between the fit and the spectrum after subtraction of a linear background. The binding energies and FWHM for the peak 2–3 region were obtained first for the spectra at 56 eV where the clearest definition of the peaks is present.

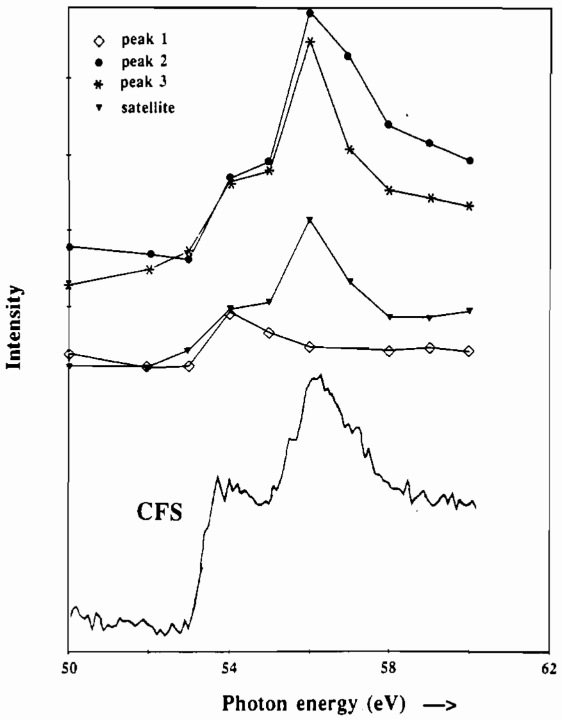

Figure 5. Absolute intensity profiles of the FeCl$_4^{2-}$ features at resonance compared to the CFS absorption spectrum (bottom).

valence electrons due to its low intensity, the remainder of the antibonding ionizations must contribute to peak 2 and thus contain dominantly d character, while peak 3 contains the dominantly Cl 3p bonding levels. The Cl 3p nonbonding levels lie in between, contributing to both peaks. This is suggested by the observed shift of the peak 2 region to lower binding energy in the 40-eV PES data in Figure 2, which indicates that the intensity on the deeper binding-energy side of peak 2 is decreasing.

Rb$_3$FeCl$_5$ photoemission spectra taken over the range 50–65 eV near the Fe 3p absorption edge are given in Figure 4, normalized to the highest peak.[19] The Rb$_3$FeCl$_5$ spectra exhibit a total of six peaks between 0- and 17-eV binding energy. The large peak at 13.5 eV has been assigned as Rb 4p$_{3/2,1/2}$ in accordance with previous work.[4b] The Rb 4p overlaps the Cl 3s level, which is at 15.7 eV. The additional feature at 9.5-eV binding energy is the satellite, which is obscured by the Cs 5p photoemission in the Cs$_3$FeCl$_5$ spectra in Figure 2. It is important to note from the 50-eV spectrum that the satellite has significant intensity (~6% of that of the main band) at nonresonance photon energies. The remaining features (peaks 1–3) are the same as for Cs$_3$FeCl$_5$. As the photon energy is swept through the Fe 3p absorption edge from 50 to 56 eV, both peak 3 and the satellite exhibit a large resonance increase in intensity. In addition, peak 1 shows a strong interference effect, decreasing in intensity from 50 to 52 eV, followed by an increase at 54 eV, and a decrease at 56 eV with a very slight increase to 57 eV.

The absolute peak intensity profiles, which were obtained from the Gaussian/Lorentzian fitting procedure described above, are given in Figure 5, along with the CFS Fe(II) 3p edge absorption spectrum. The partial yield CFS absorption edge shows a feature at 54 eV, followed by the larger feature at 56 eV. These results are qualitatively similar to those reported by Ishii for FeCl$_2$ and by Bruhn et al. for Fe vapor.[20] The peak at 54 eV has been assigned as the Fe 3p^{6}3d^6 ^{5}D → 3p^{5}3d^7 ^{5}F transition, while the feature at 56 eV corresponds to transitions to the Fe 3p^{5}3d^7 ^{5}P and ^{5}D states, where the ^{5}D is electric dipole forbidden.[21b] The profiles for peak 3 and the satellite both show resonance enhancement at 54 and 56 eV, mirroring the CFS spectrum. Peak 2 shows significant resonance as well, but the profile shape has slightly more derivative character with a dip in intensity from 50 to 53 eV. Peak 1 shows a more pronounced derivative profile for the 54-eV feature, but does not exhibit a second resonance feature at 56 eV.

Table I. Xα–SW-Calculated Ground-State Wave Functions and Transition-State Energies for FeCl$_4^{2-}$

level	ionized final states	% Fe	% Cl	Fe angular distribn	TS energy, eV	state energy
$5t_2\downarrow$	unoccupied	83	17	96% d, 4% p		
$2e\downarrow$	$^6A_1$	89	11	100% d	−1.51	
$5t_2\uparrow$	$^4T_1$, $^4T_2$	55	45	90% d, 10% p	−2.87	
$1t_1\downarrow$	$^6T_1$, $^6T_2$	0	100		−3.64	
$1t_1\uparrow$	$^4T_1$, $^4T_2$	0	100		−3.81	−3.85
$2e\uparrow$	$^4A_1$	52	48	100% d	−3.53	−3.98
	^4E					−4.45
	$^4A_2$					−5.30
$4t_2\downarrow$	$^6T_1$, $^6T_2$	8	92	81% d, 19% p	−4.24	
$1e\downarrow$	$^6A_1$, $^6A_2$, ^6E	11	89	100% d	−4.36	
$4t_2\uparrow$	$^4T_1$, $^4T_2$	11	89	42% d, 58% p	−4.61	−4.70
$3t_2\downarrow$	$^6T_1$, $^6T_2$	26	74	59% d, 41% p	−5.04	
$2a_1\downarrow$	^6E	31	69		−5.85	
$1e\uparrow$	$^4A_1$, $^4A_2$, ^4E	48	52	100% d	−5.57	−5.87
$2a_1\uparrow$	^4E	29	71		−6.29	−6.40
$3t_2\uparrow$	$^4T_1$, $^4T_2$	50	50	90% d, 10% p	−6.25	−6.55

IV. Analysis

Initial assignments of the peaks in the PE spectra in Figure 2 can be made on the basis of the absolute and relative peak intensity behavior as a function of photon energy (Figure 3). Peak 1 corresponds to ionization from the highest enery antibonding level and shows an intensity profile indicative of dominant Fe 3d character. However, the intensity of this peak is too small to contain photoemission from all six electrons present in occupied antibonding levels. Therefore, peak 1 is assigned as photoemission from the highest energy metal-derived antibonding level, with the remaining antibonding levels contributing to deeper binding energy. The absolute intensity profiles of peaks 2 and 3 in Figure 3 both show Cl 3p-like behavior, and the relative behavior indicates that peak 2 contains somewhat more Fe 3d character than peak 3. Therefore, peak 2 contains the remaining antibonding levels, which are found to have mostly Fe 3d character, and peak 3 contains photoemission from dominantly Cl 3p bonding peaks. The contribution from the Cl 3p nonbonding levels is not clearly resolved in the spectrum. More specific assignments of the PES features can be made by comparison to the results of Xα–SW calculations.

A. Ground State. 1. Wave Functions and Energies. SCF–Xα–SW calculations were performed on the FeCl$_4^{2-}$ cluster to compare results to the PE spectrum and to obtain insight into the ground-state-bonding description. The calculations were performed by using the spin-unrestricted formalism, which allows different orbitals for different spins. The results, given in Table I, show that the highest occupied antibonding level ($2e\downarrow$) contains 89% Fe 3d character. The majority spin antibonding levels are much more covalent, with 55% Fe in the $5t_2\uparrow$ level and 52% in the $2e\uparrow$ level. These spin-unrestricted calculations for the ground state correlate well with the PES results in that they reproduce the large metal character in peak 1 ($2e\downarrow$), which is separated from the more covalent spin-up antibonding levels in energy. For a quantitative comparison to the PE spectrum, the spin-unrestricted ionization energies (which include the effects of relaxation on the energy) were calculated by using the Slater transition-state method[21] (removal of 0.5 electron from a given orbital and reconvergance of the potential), and aligned with experiment at the Cl 3s level. The ionization energies obtained from the transition-state calculation for certain levels must be corrected for spin

---

(19) The Rb$_3$FeCl$_5$ valence band PES spectra were found to be identical with those for the Cs$^+$ salt at all photon energies. However, only the Rb$^+$ resonance spectra are presented, since the Rb 4p peaks do not obscure the satellite region.

(20) (a) Kakizaki, A.; Sugeno, K.; Ishii, T.; Sugawara, H.; Nagakura, I.; Shin, S. *Phys. Rev. B: Condens. Matter* **1983**, *28*, 1026. (b) Bruhn, R.; Sonntag, B.; Wolff, H.-W. *J. Phys. B.* **1979**, *12*, 203.

(21) Slater, J. C. *Adv. Quantum Chem.* **1972**, *6*, 1.

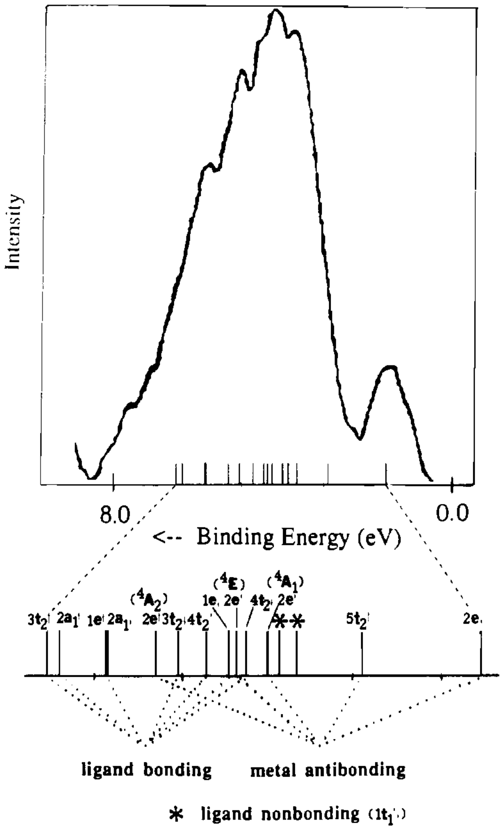

Figure 6. Comparison of calculated SCF–Xα–SW ionization energies for $FeCl_4^{2-}$ with the 40-eV PE spectrum at the Cooper minimum.

and orbital multiplet effects since they do not reflect the energy of a pure state.[22] Ionization of the 2e↓ level results in the $^6A_1$ ($m_s = {}^5/_2$) final state only. Ionization of the 5t$_2$↑ level results in $^4T_1$ and $^4T_2$ states. The splitting between the $^4T_1$ and $^4T_2$ states can be measured experimentally[26] in the ligand field spectra of d^5 $FeCl_4^-$ as 1980 cm^{-1} (0.25 eV) and can be ignored in this analysis. However, ionization from the 2e↑ level produces the final states $^4A_1$, $^4A_2$, and ^4E. The determinant calculated by the Xα method will contribute to each of these quartet states, as well as the $m_s = {}^3/_2$ component of the $^6A_1$. The Xα calculated energy was corrected by using the vector coupling method of Piepho and Schatz.[23] The expression for the formation of $|Shm\theta\rangle$ functions from two open shells is

$$|\{a^m(S_1h_1),b^n(S_2h_2)\}S_3h_3m_3\theta_3\rangle = (-1)^{S_1-S_2+2S_3-m_3}|S_3|^{1/2}\sum_{m_1m_2}\begin{pmatrix} S_1 & S_2 & S_3 \\ m_1 & m_2 & -m_3 \end{pmatrix}\times |h_3|^{1/2}\begin{pmatrix} h_3 \\ \theta_3 \end{pmatrix}\sum_{\theta_1\theta_2}\begin{pmatrix} h_1 & h_2 & h_3 \\ \theta_1 & \theta_2 & \theta_3 \end{pmatrix}|a^m(S_1m_1h_1\theta_1)\rangle|b^n(S_2m_2h_2\theta_2)\rangle \quad (1)$$

where S, h, m, and θ are the spin, orbital state, spin component, and orbital component respectively. Equation 1 was used to form the $^6A_1$, $^4A_1$, $^4A_2$, and ^4E ($m_s = {}^3/_2$) states arising from the $t_2^3e^2$ configuration. (The θ component of the ^4E state was calculated for convenience.) The determinants of interest, which appear in these wave functions in the form $|t_2^3\rangle|e^2\rangle$, are $a = |\xi^+\eta^+\zeta^+\rangle|\theta^+\epsilon^-\rangle$, $b = |\xi^+\eta^+\zeta^+\rangle|\theta^-\epsilon^+\rangle$, $c = |\xi^+\eta^+\zeta^+\rangle|\theta^2\rangle$, and $d = |\xi^+\eta^+\zeta^+\rangle|\epsilon^2\rangle$. Each of these are described by the Xα-calculated determinant, since the calculation does not distinguish between the θ and ϵ components of the e level. The wave functions for the $^6A_1$, $^4A_1$, $^4A_2$, and ^4E were combined such that all configurations dropped out except the four above. Operating on the wave function with the Hamiltonian gives eq 2. Since in the Xα calculation $E(a) = E(b)$

$$2E(^6A_1) + 3E(^4A_1) + E(^4E) + E(^4A_2) = 3E(a) + 3E(b) + {}^1\!/_2E(c) + {}^1\!/_2E(d) \quad (2)$$

$= E(c) = E(d) = E(X\alpha)$, we may group these terms together and rearrange to give eq 3. $E(X\alpha)$ and $E(^6A_1)$ are obtained directly

$${}^3\!/_7E(^4A_1) + {}^1\!/_7E(^4E) + {}^1\!/_7E(^4A_2) = E(X\alpha) - {}^2\!/_7E(^6A_1) \quad (3)$$

from the Xα calculation for the 2e↑ and 2e↓ ionization energies, respectively. The individual quartet energies can be determined by using the energy splittings for the ligand field transitions to these states in d^5 $FeCl_4^-$. The observed energy splitting between the ^4E and $^4A_1$ states is 0.47 eV, while the $^4A_2$ state was calculated to lie at 0.85 eV higher energy from the experimental ^4E value by using the Tanabe–Sugano matrices with the ferric *Dq*, *B*, and *C*.[2b] These energies are included in the last column of Table I.

The ionization energies of the spin-up ligand bonding levels must also be corrected for spin-multiplet effects. Because the repulsive interactions in this case are between a ligand hole with a metal hole, the splitting between the different orbital states may be ignored, and only the $^6\Gamma$ – $^4\Gamma$ spin correction considered. This correction was accomplished by first expanding the expression for formation of $|Shm\theta\rangle$ functions in the presence of two open shells to the expression for coupling three open shells (eq 4). Equation

$$|([a^m(S_1h_1),b^n(S_2h_2)]S_3h_3,c^l(S_4h_4))S_5h_5m_5\theta_5\rangle = (-1)^{S_1-S_2+3S_3-S_4+2S_5-m_3-m_5}|S_3|^{1/2}|S_5|^{1/2}\times \sum_{m_1m_2m_3m_4}\begin{pmatrix} S_1 & S_2 & S_3 \\ m_1 & m_2 & -m_3 \end{pmatrix}\begin{pmatrix} S_3 & S_4 & S_5 \\ m_3 & m_4 & -m_5 \end{pmatrix}\times |h_3|^{1/2}|h_5|^{1/2}\begin{pmatrix} h_3 \\ \theta_3 \end{pmatrix}\begin{pmatrix} h_5 \\ \theta_5 \end{pmatrix}\sum_{\theta_1\theta_2\theta_3\theta_4}\begin{pmatrix} h_1 & h_2 & h_3 \\ \theta_1 & \theta_2 & -\theta_3 \end{pmatrix}\begin{pmatrix} h_3 & h_4 & h_5 \\ \theta_3 & \theta_4 & -\theta_5 \end{pmatrix}\times |a^m(S_1m_1h_1\theta_1)\rangle|b^n(S_2m_2h_2\theta_2)\rangle|c^l(S_4m_4h_4\theta_4)\rangle \quad (4)$$

4 was used to form the $^6\Gamma$ and $^4\Gamma$ ($m_s = {}^3/_2$) states arising from the $|t_2^3\rangle|e^3\rangle$ d shell coupled with the $|^2\Gamma\rangle$ ligand hole ($^2T_2$, $^2T_2$, ^2E, or $^2A_1$). For the resulting T_1 and T_2 states, the *z* and ζ components were calculated for convenience, and the θ component was calculated for the E states. The determinant used in the Xα calculation for the bonding ↑ ionization is $|{}^3/_2A_2{}^3/_2\rangle|{}^1/_2E{}^1/_2\rangle|{}^1/_2\Gamma - {}^1/_2\rangle$ so only those states with $|{}^3/_2A_2{}^3/_2\rangle|{}^1/_2E{}^1/_2\rangle$ need to be obtained. These wave functions were combined such that all terms dropped out except $|a\rangle = |{}^3/_2A_2{}^3/_2\rangle|{}^1/_2E{}^1/_2\rangle|{}^1/_2\Gamma - {}^1/_2\rangle$ to give eq 5, which is appropriate for all spin-up Γ ionizations. Thus,

$$|a\rangle = \frac{1}{\sqrt{5}}[\Psi(^6\Gamma) + 2\Psi(^4\Gamma)] \quad (5)$$

the corrected $^4\Gamma$ ionization energy is obtained from eq 6. $E(a)$

$$E(^4\Gamma) = {}^5\!/_4E(a) - {}^1\!/_4E(^6\Gamma) \quad (6)$$

and $E(^6\Gamma)$ are obtained directly from the Xα calculation from the Γ↑ and Γ↓ ionization energies, respectively. Transition-state energies obtained for 1t$_1$↑, 4t$_2$↑, 1e↑, 2a$_1$↑, and 3t$_2$↑ ionization are listed under the TS energy column in Table I, while the eq 6 derived term corrected ionization energies are given in the last column. A comparison of the energies given in Table I with the 40-eV PE spectrum (Figure 6) indicates that peak 1 contains only the 2e↓ ionization; the peak 2 region contains the 5t$_2$↑ ($^4T_1$, $^4T_2$), 2e↑ ($^4A_1$), (^4E) Fe 3d antibonding, the nonbonding 1t$_1$↓,↑ ($^{6,4}T_1$, $^{6,4}T_2$), and the Cl bonding 4t$_2$↓,↑ ($^{6,4}T_1$, $^{6,4}T_2$) and 1e↓ ($^6A_1$, $^6A_2$, ^6E). The remaining Fe 3d antibonding state 2e↑ ($^4A_2$) contributes to the peak 3 region, which is dominated by the Cl 3p bonding

---

(22) (a) Bagus, P. S.; Bennet, B. I. *Int. J. Quantum Chem.* **1975**, *9*, 143. (b) Wood, J. H. *J. Phys. B* **1980**, *13*, 1. (c) Ziegler, T.; Rauk, A.; Baerends, E. J. *Theoret. Chim. Acta* **1977**, *43*, 261.

(23) Piepho, S. B.; Schatz, P. N. *Group Theory in Spectroscopy*; John Wiley and Sons, Inc.: New York, 1983. Note: Effects of the Xα multiplet averaging on the intensities of these levels were not included.

(24) (a) Gelius, U.; Siegbahn, K. *Faraday Discuss. Chem. Soc.* **1972**, *54*, 257. (b) Gelius, U. In *Electron Spectroscopy*; Shirley, D. A., Ed.; North-Holland: Amsterdam, 1972.

(25) (a) Cox, P. A.; Evans, S.; Orchard, A. F. *Chem. Phys. Lett.* **1972**, *13*, 386. (b) Cox, P. A. *Struct. Bonding* **1975**, *24*, 59.

(26) Changes in the wave functions upon ionization of the weakly bonding 4t$_2$↑ and 4t$_2$↓ were insignificant and thus also not included in the sudden approximation analysis.

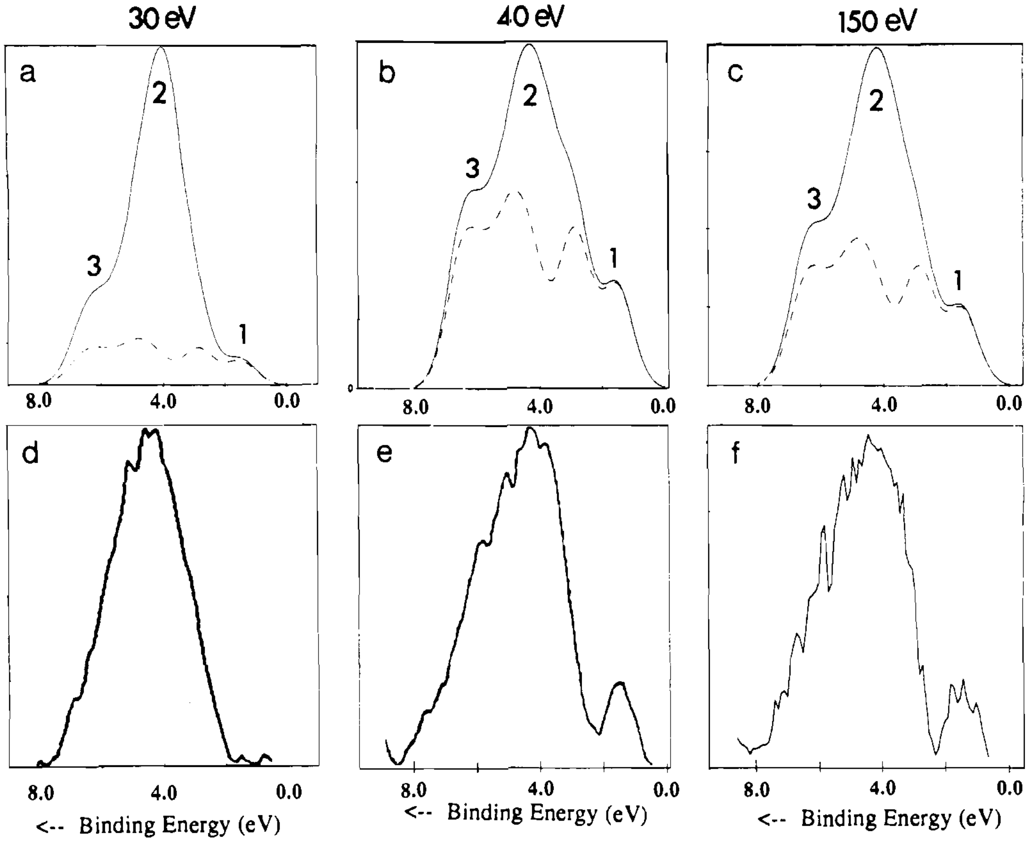

Figure 7. (a–c) SCF–Xα–SW calculated PE spectra for total intensity (—) and metal contribution only (---) at (a) 26.8, (b) 40.8, and (c) 151.2 eV. (d–f) Experimental PE spectra of FeCl$_4^{2-}$ at (d) 30, (e) 40, and (f) 150 eV.

levels 1e↑ ($^4A_1$, $^4A_2$, ^4E), 3t$_2$↓,↑ ($^{6,4}T_1$, $^{6,4}T_2$), and 2a$_1$↓,↑ ($^{6,4}E$). Thus, the peak 2–3 region is quite mixed, with metal character contributing throughout the band, but most of the metal character (5t$_2$↑ and 2e↑ ($^4A_1$, ^4E)) contributes to the lower binding energy side of peak 2 in antibonding levels.

Table II. Atomic Photoionization Cross Sections[a]

	$h\nu$ = 26.8 eV	$h\nu$ = 40.8 eV	$h\nu$ = 150 eV
Fe 3d	0.6748	1.045	0.4548
Fe 4s	0.0648	0.0650	0.0190
Cl 3p	0.5548	0.1294	0.0906

[a] Taken from ref 7a.

2. Intensities. Theoretical peak intensities were determined by using the Gelius–Siegbahn model[24] from the ground-state spin-unrestricted wave functions. The Gelius model assumes that the ionization probability of a molecular orbital (I_{mo}) is equal to the weighted sum of the ionization probabilities from its atomic orbital components (σ_{ao})

$$I_{mo} = \sum_i c_i^2 \sigma_{ao} \tag{7}$$

where the c_i's are the molecular orbital mixing coefficients. This assumption is appropriate when the input photon energy is large (≥150 eV, ensuring a high kinetic energy electron) or when one orbital cross section is much larger than the others, allowing the neglect of cross terms between metal and ligand photoionization cross sections. The latter condition is best fulfilled at the Cooper minimum at 40–50 eV, or at low photon energy where the $\sigma_{Cl\,3p}$ is at a maximum. A spectrum was generated from a sum of component Gaussians (one for each frozen orbital state with a fwhm = 1.2 eV) using the corrected Xα calculated transition-state energy from Table I and the intensity calculated for each state. Intensities were obtained by weighting the Xα wave function coefficients in Table I with the atomic Fe 3d and Cl 3p cross sections[7a] at three different photon energies (Table II) and with the appropriate fractional parentage coefficients. Any Fe 4p character appearing in the Ψ's was included with the Fe 3d character. The fractional parentage coefficients were obtained from Cox, Evans, and Orchard[25] as follows: (1) If a closed shell is ionized, all states obtained from the coupling of the positive hole with the other open shells are possible, and the relative intensities of these states are given by their spin–orbital degeneracies. (2) If the open shell is ionized, the relative probabilities of producing different states are given by the squares of the fractional parentage coefficients. Cox has tabulated the fractional parentage coefficients and relative intensities for states produced upon ionization from d^n configurations in cubic fields.[25b] The intensities of the ionized d^6 states $^4T_1$, $^4T_2$, $^6A_1$, $^4A_1$, $^4A_2$, and ^4E are $^3/_2$, $^3/_2$, $^6/_5$, $^3/_{10}$, $^1/_2$, and 1, respectively. In order for the sum of the normalized closed- and open-shell coefficients to reflect the total electron occupation, the fractional coefficients for open-shell ionization are multiplied by a factor of 5. The intensity weights and the calculated PES intensities for the three different photon energies are given in Table III; "total" intensities include both the metal and ligand contributions while "metal" intensities were obtained by setting the Cl 3p cross sections to zero. The resulting PES Gelius spectra are given in Figure 7a–C. Solid lines show the total calculated spectrum, while the dotted lines indicate the metal contribution ($\sigma_{Cl\,3p}$ = 0). The Cs$_3$FeCl$_5$ spectra taken at 30, 40, and 150 eV are given in Figure 7d–f for comparison. Overall, the agreement is very good. The calculations reproduce the general energy distribution of the intensity and the shapes of the bands. The energy and low intensity of peak 1 (2e↓) are well reproduced by the calculation, and the band 2–3 width is narrower at 30-eV photon energy. Peak 1 shows an increase in intensity from 30 to 40 eV and then a slight decrease from 40 to 150 eV. The center of the peak 2–3 band decreases in intensity from 30 to 40 eV, then increases slightly from 40 to 150 eV relative to the low-binding-energy side of peak 2 and the deeper binding-energy side of peak 3. There are, however, some quantitative differences between theory and experiment. The 40-eV spectrum shows that the low-binding-energy side of the peak 2 region where the 5t$_2$↑ contributes (see also Figure 6) is too low in energy in the theoretical spectrum. Also, the shoulder at 6–7 eV where the 3t$_2$↑ and 2a$_1$↑ contribute is too intense, and there appears to be too

Table III. Xα–SW Calculated Initial-State Intensities for $FeCl_4^{2-}$

level	intensity wt	26.8 eV		40.8 eV		151 eV	
		tot.	metal	tot.	metal	tot.	metal
$2e\downarrow$	6	3.97	3.60	5.66	5.58	2.49	2.43
$5t_2\uparrow$, ($^4T_1$, $^4T_2$)[a]	15	9.31	5.57	9.49	8.62	4.36	3.75
$1t_1\downarrow$	36	20.0		4.66		3.26	
$1t_1\uparrow$	24	13.3		3.10		2.18	
$4t_2\downarrow$	18	10.2	0.972	3.65	1.50	2.16	0.659
$2e\uparrow$ ($^4A_1$)	1.5	0.926	0.527	0.908	0.815	0.420	0.355
$1e\downarrow$	12	6.82	0.891	2.76	1.38	1.57	0.600
$4t_2\uparrow$	12	6.82	0.891	2.76	1.38	1.57	0.600
$2e\uparrow$ (^4E)	5	3.09	1.76	3.03	2.72	1.40	1.18
$3t_2\downarrow$	18	10.6	3.16	6.61	7.89	3.34	2.13
$2e\uparrow$ ($^4A_2$)	2.5	1.54	0.878	1.51	1.36	0.700	0.591
$2a_1\downarrow$	6	2.42	0.121	0.657	0.121	0.406	0.031
$1e\uparrow$	8	4.90	2.59	4.55	4.01	2.12	1.75
$2a_1\uparrow$	4	1.65	0.075	0.443	0.057	0.276	0.019
$3t_2\uparrow$	12	7.38	4.05	7.05	6.27	3.27	2.73

[a] The ^4T's are grouped together for the $5t_2\uparrow$ ionization.

Table IV. Final-State Xα–SW Calculated Wave Functions and Their Changes Relative to the Ground State (in Table I)

main ionizn	final-state levels	% Fe	ΔFe	% Cl	ΔCl
$2e\downarrow$	$5t_2\downarrow$	71	−12	29	+12
	$2e\downarrow$	76	−13	24	+13
	$5t_2\uparrow$	26	−29	74	+24
	$2e\uparrow$	12	−40	88	+40
	$1e\downarrow$	24	+13	76	−13
	$3t_2\downarrow$	34	+8	66	−8
	$1e\uparrow$	88	+40	12	−40
	$3t_2\uparrow$	76	+26	24	−26
$5t_2\uparrow$	$5t_2\downarrow$	77	−6	23	+6
	$2e\downarrow$	81	−7	19	+7
	$5t_2\uparrow$	44	−11	56	+11
	$2e\uparrow$	32	−20	68	+20
	$1e\downarrow$	19	+8	81	−8
	$3t_2\downarrow$	32	+6	68	−6
	$1e\uparrow$	68	+20	32	−20
	$3t_2\uparrow$	58	+8	42	−8
$2e\uparrow$	$5t_2\downarrow$	82	−1	18	+1
	$2e\downarrow$	83	−6	17	+6
	$5t_2\uparrow$	46	−9	54	+9
	$2e\uparrow$	34	−18	66	+18
	$1e\downarrow$	17	+6	83	−6
	$3t_2\downarrow$	31	+5	69	−5
	$1e\uparrow$	66	+18	34	−18
	$3t_2\uparrow$	56	+6	44	−6
$1e\downarrow$	$5t_2\downarrow$	80	−3	20	+3
	$2e\downarrow$	87	−2	13	+2
	$5t_2\uparrow$	54	−1	46	+1
	$2e\uparrow$	48	−4	52	+4
	$1e\downarrow$	13	+2	87	−2
	$3t_2\downarrow$	28	+2	72	−2
	$1e\uparrow$	52	+4	48	−4
	$3t_2\uparrow$	49	+1	51	−1
$3t_2\downarrow$	$5t_2\downarrow$	78	−5	22	+5
	$2e\downarrow$	86	−3	14	+3
	$5t_2\uparrow$	51	−4	49	+4
	$2e\uparrow$	41	−11	59	+11
	$1e\downarrow$	14	+3	86	−3
	$3t_2\downarrow$	29	+3	71	−3
	$1e\uparrow$	59	+11	41	−11
	$3t_2\uparrow$	52	+2	48	−2
$1e\uparrow$	$5t_2\downarrow$	69	−14	31	+14
	$2e\downarrow$	73	−16	27	+16
	$5t_2\uparrow$	45	−10	55	+10
	$2e\uparrow$	32	−20	68	+20
	$1e\downarrow$	27	+16	73	−16
	$3t_2\downarrow$	36	+10	64	−10
	$1e\uparrow$	68	+20	32	−20
	$3t_2\uparrow$	56	+6	44	−6
$3t_2\uparrow$	$5t_2\downarrow$	73	−10	27	+10
	$2e\downarrow$	78	−11	22	+11
	$5t_2\uparrow$	45	−10	55	+10
	$2e\uparrow$	32	−20	68	+20
	$1e\downarrow$	22	+11	78	−11
	$3t_2\downarrow$	33	+7	67	−7
	$1e\uparrow$	68	+20	32	−20
	$3t_2\downarrow$	56	+10	44	−10

much metal contribution (indicated by the dashed line) in this deeper binding-energy region. These discrepancies in the calculated $5t_2\uparrow$ energy and the deeper binding-energy metal intensity indicate that the Xα calculation is somewhat overestimating the covalent interaction for the spin-up levels. The effect of a decrease in spin-up mixing on the theoretical spectrum would be a slight condensing of the peak 2–3 band and a shift to lower binding energy of the metal intensity.

B. Relaxation Effects. Despite the reasonable agreement between data and theory found above, the ground-state description does not alloy for an important feature in the PE spectrum. $FeCl_4^{2-}$ exhibits significant satellite intensity at photon energies away from the resonance, in contrast to the d^5 $FeCl_4^-$. The satellite corresponds to a two-electron process, which is forbidden within the ground-state frozen-orbital approximation, but should gain intensity through relaxation, which changes the final state wave functions: The greater the relaxation, the larger the off-resonance satellite intensity. The satellite in the $FeCl_4^{2-}$ spectrum in Figure 8 contains 6% of the total main-band intensity measured at 50-eV input photon energy, indicating that substantial relaxation is occurring on ionization. The ground-state results for $FeCl_4^{2-}$ in section IVA indicate a normal molecular orbital description that has the antibonding levels derived mostly from metal orbitals. However, this is in strong contrast to our previous results on high-spin d^5 T_d $FeCl_4^-$, which exhibits an inverted ground-state-bonding scheme with the metal-derived occupied levels at a deeper binding energy from those of the ligand.[3] The large exchange splitting in high-spin d^5 was determined to be the origin of this unusual bonding. As the exchange splitting is not as large in the d^6 ground state, d ionization should result in a significant increase in the exchange interaction. Our previous study on $CuCl_4^{2-}$ also showed a large relaxation in the final state, in which the satellite had 9% of the main-band intensity at 50 eV.[4a] However, in Cu^{2+} ionization, the relaxation is largely due to the change in Coulomb repulsion on ionization, which will also be present, although smaller, in Fe^{2+} ionization. These relaxation effects, including the contributions of electron repulsion and exchange, were investigated by using the spin-unrestricted SCF–Xα–SW calculations for the final states.

1. Wave Functions and Energies. Relaxed final-state wave functions were obtained for each orbital ionization by removing one electron and reconverging the potential. The resulting coefficients for the orthonormal Ψ's for the levels involved in bonding are given in Table IV. Comparison of the relaxed final states to the ground-state calculation in Table I (ΔFe and ΔCl values in Table IV) shows significant changes occur in the wave functions upon ionization, particularly in the spin-up levels where the bonding interaction is greater. These changes are the result of a rearrangement of the electron density in response to the creation of a valence hole. Ionization of the $2e\downarrow$, $5t_2\uparrow$, $2e\uparrow$, $1e\uparrow$, or $3t_2\uparrow$ causes a substantial loss of metal character in the antibonding levels, particularly in the $5t_2\uparrow$ and $2e\uparrow$, which become ligand based in the final state. The metal character is shifted to the bonding ligand levels: the $3t_2\uparrow$ and $1e\uparrow$ become dominantly metal, and the $3t_2\downarrow$ and $1e\downarrow$ also gain some metal character (but are still predominantly ligand). Ionization from the $3t_2\downarrow$ and $1e\downarrow$ bonding levels produces significant, but less dramatic results. Ionization from the nonbonding levels produces no change in the wave functions as the absence of d-orbital prevents charge flow between the Fe sphere and the Cl sphere.[26]

The changes observed in the one-electron-ionized wave functions are responsible for the appearance of intensity in the satellite at photon energies away from resonance. Energies for the shakeup satellite states were determined by using the Slater transition-state method[21] by removing one valence electron and then transferring 0.5 electron from the ligand to the metal level. The energy difference between these fractionally occupied levels is added to

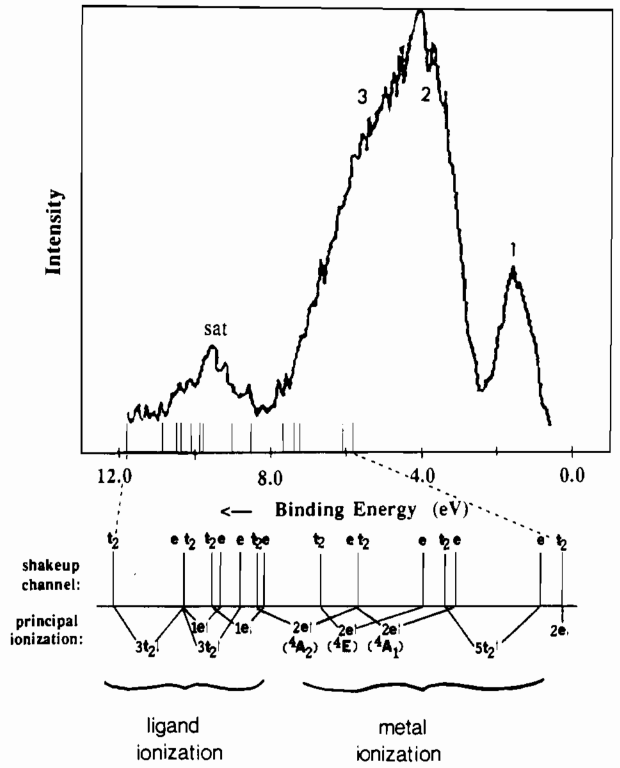

Figure 8. Comparison of calculated SCF–Xα–SW shakeup energies with the 50-eV PE spectrum.

Table V. Xα–SW Calculated Satellite Ionization Energies for FeCl$_4^{2-}$

level	main ionizn, eV	satellite energies, eV	
		e shakeup	t$_2$ shakeup
$2e\downarrow$	1.51		5.80
$5t_2\uparrow$	2.87	6.06	7.35
$2e\uparrow$ ($^4A_1$)	3.98	7.19	8.51
$1e\downarrow$	4.36	9.75	10.44
$2e\uparrow$ (^4E)	4.45	7.66	8.98
$3t_2\downarrow$	5.04	10.07	10.80
$2e\uparrow$ ($^4A_2$)	5.30	8.51	9.83
$1e\uparrow$	5.87	10.33	10.80
$3t_2\uparrow$	6.55	10.83	11.74

the ionization energy of the main line to give the satellite binding energy (Table V). The energies corresponding to $1e\downarrow \rightarrow 2e\downarrow$ and $3t_2\downarrow \rightarrow 5t_2\downarrow$ shakeup with the principal ionizations of $5t_2\uparrow$, $2e\uparrow$ ($^4A_1$, $^4A_2$, and ^4E), $1e\uparrow,\downarrow$, and $3t_2\uparrow,\downarrow$, and the $3t_2\downarrow \rightarrow 5t_2\downarrow$ shakeup for the $2e\downarrow$ ionization (note that $2e\downarrow$ plus $1e\downarrow \rightarrow 2e\downarrow$ shakeup produces the same final state as $1e\downarrow$ ionization) were calculated, resulting in a total of 17 satellite states. Figure 8 gives the expanded PE spectrum with the calculated satellite energies identified at the bottom. Five of the satellite states have calculated binding energies that place them in the peak 3 region of the spectrum (<8.0 eV): $2e\downarrow$ ($3t_2\downarrow \rightarrow 5t_2\downarrow$), $5t_2\uparrow$ ($1e\downarrow \rightarrow 2e\downarrow$ and $3t_2\downarrow \rightarrow 5t_2\downarrow$), $2e\uparrow$-$4A_1$ ($1e\downarrow \rightarrow 2e\downarrow$), and $2e\uparrow$-^4E ($1e\downarrow \rightarrow 2e\downarrow$). All five involve ionization from the Fe 3d antibonding levels. The remaining four Fe 3d antibonding ionization plus shakeup states of $2e\uparrow$-$^4A_1$ ($3t_2\downarrow \rightarrow 5t_2\downarrow$), $2e\uparrow$-^4E ($3t_2\downarrow \rightarrow 5t_2\downarrow$), and $2e\uparrow$-$^4A_2$ ($1e\downarrow \rightarrow 2e\downarrow$) contribute to the low-energy side of the satellite (the $2e\uparrow$-$^4A_2$ ($3t_2\downarrow \rightarrow 5t_2\downarrow$) at 9.83 eV is at the center of the satellite). The remaining eight satellite states correspond to $1e\downarrow$, $3t_2\downarrow$, $1e\uparrow$, and $3t_2\uparrow$ ligand ionization plus ligand to metal shakeup (both $1e\downarrow \rightarrow 2e\downarrow$ and $3t_2\downarrow \rightarrow 2t_2\downarrow$) and are calculated to contribute from 9.75 to 11.74 eV, in general agreement with the position of the satellite. In the next section, these ligand ionization plus shakeup states are found to have most of the intensity and are responsible for the observed satellite peak.

Table VI. Intensity Redistribution from the Sudden Approximation

(a) t$_2$ Shakeup

main ionizn	redistributed intensity			
	Ψ_1 (metal)	Ψ_3 (metal plus $3t_2\downarrow \rightarrow 5t_2\downarrow$ shakeup)	Ψ_2 (ligand)	Ψ_4 (ligand plus $3t_2\downarrow \rightarrow 5t_2\downarrow$ shakeup)
$2e\downarrow$	0.934	0.036	0.029	1.2×10^{-3}
$5t_2\uparrow$	0.954	0.029	0.016	5.5×10^{-4}
$2e\uparrow$	0.942	0.025	0.032	8.7×10^{-4}
$1e\downarrow$	9.0×10^{-4}	1.8×10^{-5}	0.981	0.018
$3t_2\downarrow$	2.2×10^{-3}	4.8×10^{-5}	0.977	0.021
$1e\uparrow$	0.39	2.0×10^{-3}	0.915	0.044
$3t_2\uparrow$	2.5×10^{-3}	8.8×10^{-5}	0.964	0.033

(b) e Shakeup

main ionizn	redistributed intensity			
	Ψ_1 (metal)	Ψ_3 (metal plus $1e\downarrow \rightarrow 2e\downarrow$ shakeup)	Ψ_2 (ligand)	Ψ_4 (ligand plus $1e\downarrow \rightarrow 2e\downarrow$ shakeup)
$2e\downarrow$	0.969		0.030	9.2×10^{-4}
$5t_2\uparrow$	0.970	0.013	0.017	2.2×10^{-4}
$2e\uparrow$	0.960	7.0×10^{-3}	0.033	2.6×10^{-4}
$1e\downarrow$	9.3×10^{-4}		0.998	9.3×10^{-4}
$3t_2\downarrow$	2.3×10^{-3}	7.2×10^{-6}	0.996	2.1×10^{-3}
$1e\uparrow$	0.039	1.7×10^{-3}	0.918	0.041
$3t_2\uparrow$	2.5×10^{-3}	5.2×10^{-5}	0.975	0.022

2. Intensities. Changes in the wave functions upon ionization can be used to calculate the redistribution of photoemission intensity in the relaxed final state out of resonance. The frozen-orbital final states are expanded in terms of the relaxed final states of the ion by using the sudden approximation

$$\Psi_R(N-1) = \sum_i \langle \Psi_i | \Psi_R \rangle \Psi_i(N-1) \tag{8}$$

where $\Psi_R(N-1)$ is the remainder wave function of the frozen-orbital state after one-electron ionization and the $\Psi_i(N-1)$ are the ground and excited states of the relaxed ion.[6] The total intensity for the $\Psi_R(N-1)$ frozen-orbital state (Table III) is thus partitioned among all the possible final states of the relaxed ion. For example, the ionization of the $5t_2\uparrow$ state can result in four possible final states, the product hole wave functions for which are given in eq 9. These product wave functions are calculated

$$\begin{aligned} \Psi_1 &= (5t_2\uparrow)(2e\downarrow) \\ \Psi_2 &= (3t_2\uparrow)(2e\downarrow) \\ \Psi_3 &= (5t_2\uparrow)(1e\downarrow) \\ \Psi_4 &= (3t_2\uparrow)(1e\downarrow) \end{aligned} \tag{9}$$

by using the relaxed Ψ's in Table IV and then projecting onto the $\Psi_R = (5t_2\uparrow)(2e\downarrow)$ from the spin-unrestricted frozen-orbital wave functions in Table I. The squares of the $\langle \Psi_i | \Psi_R \rangle$ overlap integrals give the percentage of intensity that (a) remains in the $5t_2\uparrow$ metal ionization (Ψ_1), (b) is shifted to the main band $3t_2\uparrow$ ligand ionization (Ψ_2), or (c) is redistributed into the satellite region (metal ionization plus shakeup Ψ_3, and ligand ionization plus shakeup Ψ_4).

Results of the intensity redistribution for the two shakeup channels are given in Table VIa,b. The theoretical relaxed spectrum is given in Figure 9a (which includes the frozen orbital intensity calculation as a reference), along with a comparison to the 50-eV experimental spectrum (Figure 9b). Most of the intensity remains in peaks 1–3; however, 3% of the total main-band intensity is shifted into the satellite states. A very small (3%) redistribution between the main peaks also occurs. The two satellite states predicted to lie under peak 3 in Figure 8 have a negligible effect on the spectrum. Of the satellite states to deeper binding energy from the main band, more intensity (62% of the total satellite intensity) is shifted to the ligand ionization plus shakeup states than the satellites from metal ionization, and the ligand ionization shakeup states have the intensity concentrated into a peak in the experimental satellite region. Thus, these results show a small, but important, difference from the ground-state analysis. While most of the intensity remains in the main-band peaks, 3% is calculated to shift into the satellites due to relaxation.

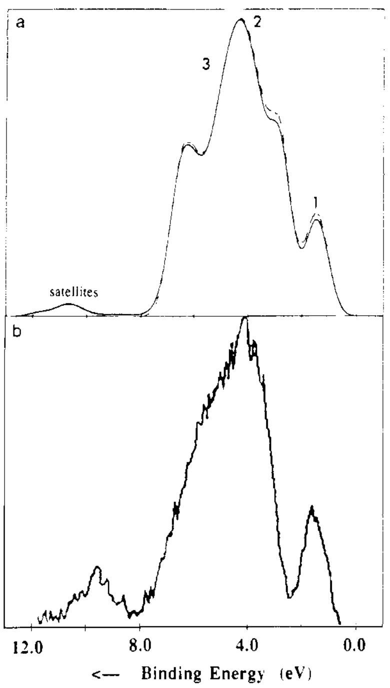

Figure 9. (a) Relaxed SCF-Xα-SW-calculated PE spectrum using the sudden approximation at the Cl 3p Cooper minimum (frozen spectrum indicated by dashed line). (b) PE spectrum of Rb_3FeCl_5 at 50 eV.

This is to be compared to the 6% observed experimentally. In our previous study on $CuCl_4^{2-}$, which exhibits substantial relaxation upon ionization, the experimental satellite intensity was 9% of the main band, compared to 5% predicted by the sudden approximation.[4a] In addition, the $CuCl_4^{2-}$ calculation showed more redistribution of intensity (10–20%) within the main band. Thus, the extent of relaxation appears to be similar, but somewhat more limited in ferrous than cupric chloride, and can be quantified by comparison of the Xα calculated changes in wave function for these two complexes. From Table IV, ionization from the HOMO 2e$\downarrow$ produces a decrease of 23% Fe character averaged over the antibonding orbitals, while ionization from the HOMO $3b_{1g}$ in D_{4h} $CuCl_4^{2-}$ produces a loss of 33% Cu averaged over the antibonding orbitals. On the basis of free ion values, the change in electron repulsion for Fe^{2+} should be less than than for Cu^{2+} due to its lower effective nuclear charge (free ion values: Cu = 16.5 eV, Fe = 14.5 eV).[27] The significant magnitude of the ferrous relaxation likely also involves a large exchange contribution.

C. Resonance Effects. The behavior of the PE spectral features at the resonance absorption edge provides an additional probe of the location of metal character in the relaxed levels of the final state and hence a measure of the extent of relaxation on ionization. From Figure 4, the main resonance enhancement occurs in peak 3; however, significant enhancement also occurs in the satellite as well as peaks 1 and 2. While peak 3 and the satellite show an enhancement line shape, peaks 1 and 2 show a derivative-like profile (Figure 5). The relative intensities of peaks 2 and 3 and the satellite in ferrous chloride are, in fact, very similar to the resonance intensities of peaks 1 and 3 and the satellite in ferric chloride, which also showed dominant resonance enhancement in peak 3. A comparison of the resonance profiles for both complexes is given in Figure 10. (Note peak 2 in ferrous chloride is analogous to peak 1 in the ferric complex. See ref 3 for details.) The ferric chloride complex does not exhibit relaxation on ionization, and thus its resonance spectrum reflects the initial-state covalent mixing, which can then be qualitatively compared to the ferrous final-state wave functions as revealed by the resonance profiles in Figure 10. The origin of the peak 3 and satellite resonance intensity in ferric chloride is the inverted-bonding description present in this complex, which places dominant metal character in the bonding levels in the initial state. The similarity between the resonance spectra of ferric and ferrous chloride then indicates that the ferrous final-state-bonding description is inverted from that of the ferrous chloride ground state, thus shifting the metal character from peaks 1 and 2 into peak 3 and the satellite. The presence of significant resonance enhancement in the main band differs from the results for $CuCl_4^{2-}$, which showed the largest enhancement in the satellite, with only limited resonance in the main band. Thus, the resonance PES results on $FeCl_4^{2-}$ indicate again that the relaxation in ferrous chloride is more limited than that in cupric chloride; however, the off-resonance satellite data in section B above clearly indicate that significant relaxation does occur, and the similarity of the ferrous chloride resonance to that of ferric chloride demonstrates that the relaxation produces an inverted-bonding scheme in the final state.

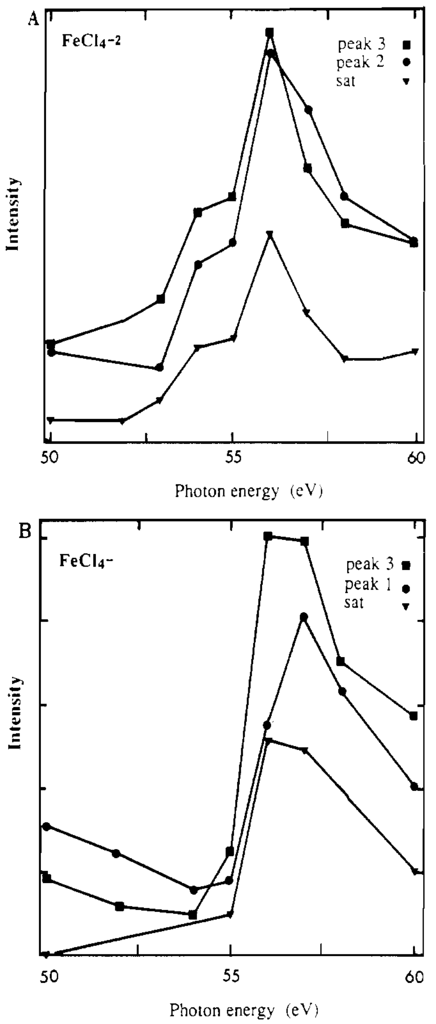

Figure 10. Comparison of the experimental resonance intensity profiles for (A) $FeCl_4^{2-}$ and (B) $FeCl_4^-$. (Note that peak 2 in the ferrous chloride is equivalent to peak 1 in ferric chloride.)

The complete experimental resonance profiles in Figure 5 show that, in contrast to the other PES features, peak 1 is enhanced at 54 eV, but not at 56 eV. This was also observed for octahedral $FeCl_2$ in a study by Ishii et al.[20a] The assignment of the CFS absorption edge and the final states accessible through the Auger decay provide insight into this unusual behavior. The first feature at 54 eV is assigned as the Fe $3p^63d^6$ $^5D \rightarrow 3p^53d^7$ ^5F transition, while the feature at 56 eV corresponds to the $3p^63d^6 \rightarrow 3p^53d^7$ ^5P and ^5D states. The ^5F, ^5P, and ^5D ferrous excited states will decay so as to conserve angular momentum. Direct ionization of the 2e$\downarrow$ corresponds to ^5D $d^6 \rightarrow$ ^6S d^5 plus an f-wave continuum electron, ϵl (the L-1 channel, resulting in a p-wave electron, has low probability). The ^6S ϵf final state produced by this ionization, which corresponds to peak 1, can only be reached through Auger

---

(27) (a) Brandow, B. H. *Adv. Phys.* **1977**, *26*, 651. (b) Moore, C. E. *Atomic Energy Levels*; U.S. National Bureau of Standards Circular 467; U.S. Government Printing Office: Washington, DC, 1952.

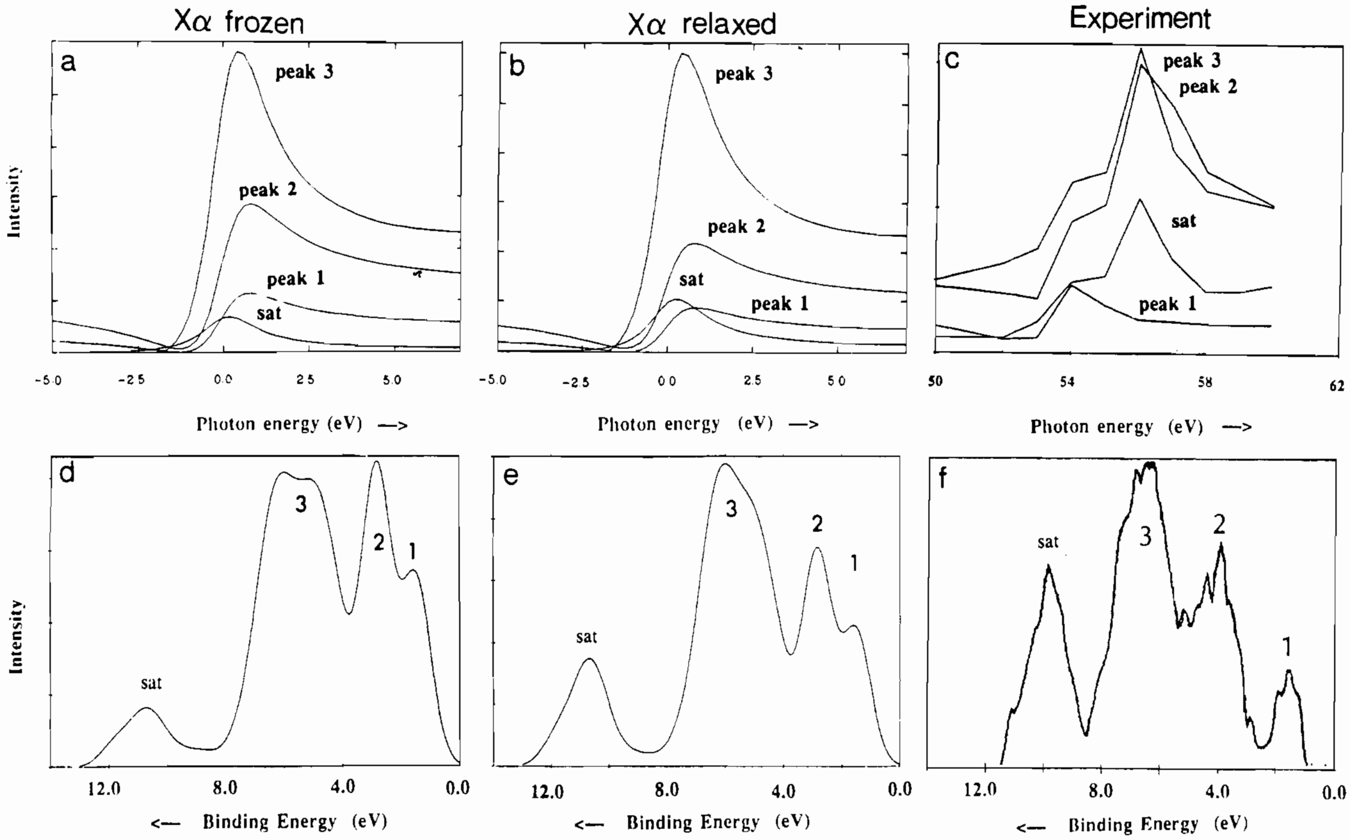

Figure 11. (a–c) Theoretical resonance profiles for FeCl$_4^{2-}$ obtained by using SCF–Xα–SW results within the Davis formalism: (a) frozen wave functions; (b) relaxed wave functions; (c) experimental metal-only resonance profiles. (d–f) Theoretical resonance spectra at $\epsilon = 1$ eV: (d) frozen wave functions; (e) relaxed wave functions; (f) experimental resonance difference spectrum.

decay of the ^{5}F excited state ($3p^53d^7\ {}^5F \rightarrow 3p^63d^5\ {}^6S + \epsilon f$), and thus enhancement of this state is not accessible at the ^{5}P, ^{5}D edge. Only the 2e↓ (^{6}S εf) final state has this restriction; all the remaining $^4\Gamma$ ionized final states can be reached from ferrous excited states in both absorption edge features.

In order to obtain further insight from the resonance profiles and to assess the accuracy of the Xα calculation, we have produced theoretical resonance spectra and profiles using the Xα wave functions and the resonance intensity formalism of Davis.[9] This intensity formalism considers a one-hole ground state, which can either be in the unoccupied 2e↓ level or the 5t$_2$↓ level.

The wave function for a one-hole ground state is

$$\Psi_g = \cos\theta|\underline{d}\rangle - \sin\theta|\underline{L}\rangle \qquad (10)$$

where $|\underline{d}\rangle$ and $|\underline{L}\rangle$ denote one hole on the metal and one on the ligand, respectively. Ionization of a valence electron creates a second hole, producing one triplet state and three singlets. The singlet states are of the form

$$\Psi_s = \alpha(|\underline{d}{\uparrow}\underline{L}{\downarrow}\rangle + |\underline{d}{\downarrow}\underline{L}{\uparrow}\rangle) + \beta|\underline{d}^2\rangle + \gamma|\underline{L}^2\rangle \qquad (11)$$

with normalization condition $2\alpha^2 + \beta^2 + \gamma^2 = 1$. The emission from the three singlet states, k, can be written as

$$N_k = \left(\alpha_k \sin\theta + \beta_k(\cos\theta)\frac{\epsilon + q}{\epsilon + i}\right)^2 \qquad (12)$$

$$\epsilon = \frac{h\nu - h\nu_0}{\Gamma} \qquad (13)$$

where $h\nu$ is the photon energy, $h\nu_0$ is the energy at resonance, $2\Gamma = 2\pi V_{\rm sck}^2$ is the super-Coster–Kronig (SCK) decay width (fwhm), and q is the Fano asymmetry parameter

$$q = \frac{\langle 3d|r|3p\rangle}{\pi V_{\rm sck}^2\langle \epsilon l|r|3d\rangle} \qquad (14)$$

The second term in eq 12 is responsible for the resonance modulation.

The ionized two-hole Xα wave functions (both frozen-orbital and relaxed) generated in section B2 (for example, in eq 9) for the sudden approximation analysis are of the same form as in eq 11 and were used here with eq 12 to produce a separate resonance profile for each state. The cos θ term involving the e channel is 0.943 from the 2e↓ initial-state mixing ($\cos^2\theta = 0.89$ Fe in Table I). Those states involving shakeup in the t$_2$ channel have a 5t$_2$↓ $\cos\theta = 0.911$. The α and β values in eq 12 were obtained from the two-hole Xα wave functions (eq 9, etc.), and are listed in parts a (frozen) and b (relaxed) of Table VII. The phase was chosen to be consistent with the Xα wave functions and the correct line shape. A value of 1.5 was used for q in eq 12, and each state was weighted by using the coefficients in the Gelius ground-state analysis. These calculated resonance intensities were then used to simulate the theoretical PE spectra and resonance profiles at the absorption edge.

Theoretical resonance profiles for peaks 1–3 and the satellite were produced by summing the individual weighted profiles (described above) that contribute to each feature. Peak 1 contains the 2e↓ profile only, peak 2 is assigned the states between 2.87 and 4.45 eV, peak 3 covers 5.04–7.99 eV, and all states deeper than 7.99 eV are included in the satellite profile (see Tables I and V). The resulting profiles using both frozen and relaxed Xα wave functions are given in parts a and b of Figure 11, respectively. The experimental resonance profiles are reproduced in Figure 11c with the ligand contribution subtracted, since eq 12 does not include the ligand cross section contributions.[28] The intensities and shapes of the experimental profiles (compared at the 54-eV edge only, since peak 1 does not show resonance at 56 eV and only one resonance absorption edge was used in the calculations) are generally reproduced by both the frozen and relaxed Xα-calculated profiles: the relaxed profiles reproduce the correct

---

(28) The amount of ligand intensity in peaks 1, 2, and 3 was estimated from the difference in Xα intensities for total and metal contributions at 40 eV given in Table III. The satellites were treated as having only metal character since their total off-resonance intensity is small.

Table VII. Resonance Intensity Parameters for Xα Wave Functions

two-hole wave function	cos θ	α	β
(a) Frozen Xα Wave Functions			
$(2e\downarrow)(2e\downarrow)$	0.943	0.313	0.890
$(2e\downarrow)(5t_2\downarrow)$	0.911	0.346	0.859
$(2e\downarrow)(1e\downarrow)$	0.943	−0.500	0.313
$(2e\downarrow)(3t_2\downarrow)$	0.911	−0.491	0.481
$(5t_2\uparrow)(2e\downarrow)$	0.943	0.440	0.700
$(5t_2\uparrow)(5t_2\downarrow)$	0.911	0.459	0.676
$(5t_2\uparrow)(1e\downarrow)$	0.943	−0.461	0.246
$(5t_2\uparrow)(3t_2\downarrow)$	0.911	−0.490	0.378
$(2e\uparrow)(2e\downarrow)$	0.943	0.447	0.680
$(2e\uparrow)(5t_2\downarrow)$	0.911	0.464	0.657
$(2e\uparrow)(1e\downarrow)$	0.943	−0.455	0.239
$(2e\uparrow)(3t_2\downarrow)$	0.911	−0.487	0.368
$(1e\downarrow)(2e\downarrow)$	0.943	−0.500	0.313
$(1e\downarrow)(5t_2\downarrow)$	0.911	−0.498	0.302
$(1e\downarrow)(1e\downarrow)$	0.943	−0.313	0.110
$(1e\downarrow)(3t_2\downarrow)$	0.911	−0.383	0.169
$(3t_2\downarrow)(2e\downarrow)$	0.943	−0.491	0.481
$(3t_2\downarrow)(5t_2\downarrow)$	0.911	−0.497	0.465
$(3t_2\downarrow)(1e\downarrow)$	0.943	−0.383	0.169
$(3t_2\downarrow)(3t_2\downarrow)$	0.911	−0.439	0.260
$(1e\uparrow)(2e\downarrow)$	0.943	−0.455	0.654
$(1e\uparrow)(5t_2\downarrow)$	0.911	−0.472	0.631
$(1e\uparrow)(1e\downarrow)$	0.943	−0.447	0.230
$(1e\uparrow)(3t_2\downarrow)$	0.911	−0.482	0.353
$(3t_2\uparrow)(2e\downarrow)$	0.943	−0.451	0.667
$(3t_2\uparrow)(5t_2\downarrow)$	0.911	−0.468	0.644
$(3t_2\uparrow)(1e\downarrow)$	0.943	−0.451	0.235
$(3t_2\uparrow)(3t_2\downarrow)$	0.911	−0.485	0.361
(b) Relaxed Xα Wave Functions			
$(2e\downarrow)(2e\downarrow)$	0.943	0.427	0.760
$(2e\downarrow)(5t_2\downarrow)$	0.911	0.441	0.735
$(2e\downarrow)(1e\downarrow)$	0.943	−0.500	0.427
$(2e\downarrow)(3t_2\downarrow)$	0.911	−0.497	0.508
$(5t_2\uparrow)(2e\downarrow)$	0.943	0.481	0.597
$(5t_2\uparrow)(5t_2\downarrow)$	0.911	0.488	0.582
$(5t_2\uparrow)(1e\downarrow)$	0.943	−0.462	0.289
$(5t_2\uparrow)(3t_2\downarrow)$	0.911	−0.485	0.375
$(2e\uparrow)(2e\downarrow)$	0.943	0.490	0.531
$(2e\uparrow)(5t_2\downarrow)$	0.911	0.492	0.528
$(2e\uparrow)(1e\downarrow)$	0.943	−0.433	0.240
$(2e\uparrow)(3t_2\downarrow)$	0.911	−0.468	0.325
$(1e\downarrow)(2e\downarrow)$	0.943	−0.500	0.336
$(1e\downarrow)(5t_2\downarrow)$	0.911	−0.498	0.322
$(1e\downarrow)(1e\downarrow)$	0.943	−0.336	0.130
$(1e\downarrow)(3t_2\downarrow)$	0.911	−0.400	0.191
$(3t_2\downarrow)(2e\downarrow)$	0.943	−0.491	0.499
$(3t_2\downarrow)(5t_2\downarrow)$	0.911	−0.499	0.476
$(3t_2\downarrow)(1e\downarrow)$	0.943	−0.407	0.201
$(3t_2\downarrow)(3t_2\downarrow)$	0.911	−0.454	0.290
$(1e\uparrow)(2e\downarrow)$	0.943	−0.456	0.705
$(1e\uparrow)(5t_2\downarrow)$	0.911	−0.465	0.685
$(1e\uparrow)(1e\downarrow)$	0.943	−0.500	0.428
$(1e\uparrow)(3t_2\downarrow)$	0.911	−0.500	0.495
$(3t_2\uparrow)(2e\downarrow)$	0.943	−0.468	0.661
$(3t_2\uparrow)(5t_2\downarrow)$	0.911	−0.478	0.639
$(3t_2\uparrow)(1e\downarrow)$	0.943	−0.486	0.351
$(3t_2\uparrow)(3t_2\downarrow)$	0.911	−0.497	0.430

intensity order at the absorption edge (0 eV) as that experimentally observed at 54 eV, with peak 3 dominant, followed by peak 2, satellite, and peak 1. Both peak 3 and the satellite show positive enhancement, while peaks 1 and 2 show derivative shapes that increase in intensity at photon energies above that at which peak 3 and the satellite have reached maximum enhancement.

Theoretical resonance PE spectra were generated by taking the weighted intensities for each individual state at $\epsilon = 1$ eV, and subtracting the value obtained for the nonresonance spectrum (estimated by using $\epsilon = -15$ eV). Figure 11 shows the resulting spectra for the frozen-orbital wave functions (11d) and the relaxed wave functions (11e). Comparing the calculated frozen spectrum to the relaxed spectrum shows that relaxation shifts significant resonance intensity into the satellite. This is also observed in a quantitative comparison of the Xα frozen and relaxed resonance profiles. Figure 11f shows the experimental resonance spectrum (i.e. the difference between 55 and 50 eV). This experimental difference spectrum shows large resonance in peak 3, with substantial enhancement in the satellite, peak 2, and peak 1. Comparison of the relaxed Xα-calculated spectrum with the experimental data indicates that the theoretical spectrum overestimates the resonance in peak 3 relative to the other three features, particularly peak 2 and the satellite. This discrepancy is reproduced in the theoretical Xα relaxed profile, and is indicative of too much metal character in the final states contributing to the peak 3 region. Again, the Xα calculation appears to somewhat overestimate the amount of covalent mixing in the spin-up levels. The most important feature in these profiles is the change from the Xα frozen to the relaxed profile, which causes a large increase in the satellite resonance (with peak 3 retaining the dominant enhancement). This is consistent with the experimental satellite resonance and is indicative of significant relaxation in this system, which inverts the bonding description from the ground to the final state.

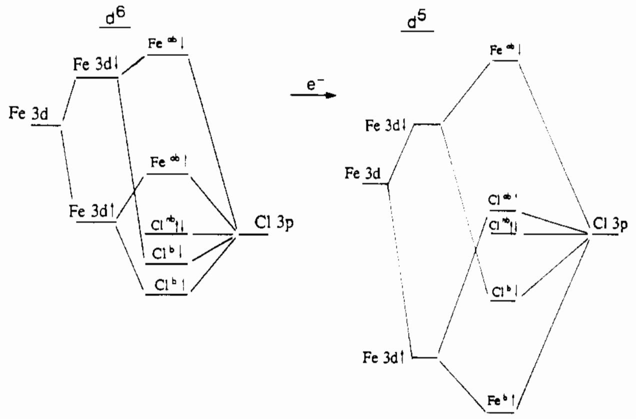

Figure 12. Comparison of the energy-level diagram for high-spin d^6 $FeCl_4^{2-}$ with that of high-spin d^5 $FeCl_4^-$, including the effects of spin polarization and relaxation on ionization.

V. Discussion

These variable-energy PES results have revealed important differences in bonding between high-spin ferrous and ferric systems. The behavior of the $FeCl_4^{2-}$ peak intensities as a function of photon energy through the Cl 3p Cooper minimum (Figure 2) indicates that the HOMO (peak 1) is localized on the metal. The remaining antibonding levels (peak 2) appear to significantly deeper binding energy and are more covalent, but still contain more metal than ligand character. The difference in covalency for these levels is evident in the absolute intensity profiles, which show Fe 3d behavior for peak 1, but Cl 3p behavior for peak 2. Although these results conform to the normal bonding description for transition-metal complexes, it is apparent that exchange effects are playing an important role in determining the covalent mixing. The spin-unrestricted Xα calculations reproduce the experimental PES behavior, showing substantial differences in covalency between the spin-up and spin-down counterparts of antibonding levels (Table I). The spin-unrestricted bonding description, which is thus experimentally and theoretically found to be present in high-spin d^6 systems, is shown schematically in Figure 12 (left) and compared to the bonding description for high-spin d^5 in Figure 12 (right). Exchange splitting stabilizes the Fe 3d↑ levels, shifting them closer to the ligand levels in energy, resulting in a larger covalent interaction ($Fe^{ab}\uparrow$, peak 2). The occupied Fe 3d↓ ($Fe^{ab}\downarrow$, peak 1) is a spin-down HOMO that is largely localized on the metal and separated in energy from the rest of the antibonding levels. With respect to final-state effects, the valence-band spectrum shows a satellite peak (Figure 4), which contains 6% of the total main-band intensity at nonresonance photon energies. This satellite has been assigned on the basis of Xα calculations of its energy and intensity as a ligand ionization plus ligand-to-metal charge-transfer shakeup transition. The presence of off-

Table VIII. Percent Fe Character for $2e\downarrow$ Ionized Xα–SW Wave Functions for Different Sphere Radii and Bond Lengths

	ferrous radii and bond lengths	ferric radii and ferrous bond lengths	ferric radii and bond lengths
$5t_2\downarrow$	71	74	74
$2e\downarrow$	76	81	80
$5t_2\uparrow$	26	26	36
$2e\uparrow$	12	13	21
$1e\downarrow$	24	19	20
$3t_2\downarrow$	34	30	31
$1e\uparrow$	88	87	79
$3t_2\uparrow$	76	74	65

resonance satellite intensity indicates that significant relaxation is occurring in ferrous chloride upon ionization. Final-state relaxation is also indicated by the presence of dominant resonance enhancement in peak 3 (corresponding to $Cl^b\uparrow$ in the initial state in Figure 12 (left)) rather than in peaks 1 and 2.

While the bonding in ferrous chloride reflects a normal covalent ground state, this is not the case for ferric chloride. In the ferric system, the Fe 3d↑ levels in Figure 12 (right) drop below the Cl 3p, thus producing an inverted bonding scheme for the Fe↑ levels in the ground state. This inversion is a consequence of the decrease in electron repulsion combined with the increase in the exchange interaction on going from high-spin Fe(II) to Fe(III). Thus, the ground-state-bonding descriptions of these two systems are very different, yet the lowest energy ionized ferrous chloride final state should be related to the ferric chloride ground state. Because ferric chloride does not show relaxation on ionization,[3] the resonance spectra reflect the metal character in both the final and ground states and can thus be compared to the ferrous chloride resonance spectra, which reflect the effects of final-state relaxation. Comparison of these resonance spectra in Figure 10 shows that the shapes of the resonance profiles and the order of intensities in ferrous chloride are very similar to those of ferric chloride. This indicates that the bonding description in the ionized ferrous final state has relaxed sufficiently to become inverted due to the change in electron repulsion and exchange, with the HOMO ($5t_2\uparrow$) now being mostly ligand in character ($Cl^b\uparrow$ in Figure 12 (right)).

Photoionization of the $2e\downarrow$ electron directly relates to oxidation processes in ferrous complexes. As stated above, the $2e\downarrow$ ionized final state should be related to the ground state in ferric chloride. According to the Xα wave functions, the ionized final state of ferrous chloride is somewhat less covalent than calculated for the ferric chloride ground state.[3] These calculations differ both in the bond lengths of the ferric vs ferrous complexes and in the sphere sizes required for the scattered wave calculation to be adjusted to experimental data (vida supra). In order to evaluate the relative effects of changes in bond lengths and sphere sizes on this mixing, an intermediate calculation was performed for $2e\downarrow$ ionization which had the ferrous bond lengths with the ferric sphere radii. From Table VIII, the change in the bond length (with ferric sphere radii) had little effect on the spin-down levels, but makes the spin-up levels considerably less covalent by 8–10%. Changing to the ferrous sphere radii has no effect on the spin-up levels and causes only a slight increase in spin-down covalency. Thus, the longer Fe–Cl bond length in ferrous chloride, which does not relax on the PES time scale, is responsible for the somewhat descreased covalent mixing in the ionized final state of the ferrous relative to the ground state of the analogous ferric complex.

The electronic contributions to redox processes can be greatly altered by electronic relaxation. Relaxation on ionization stabilizes the final state and thus makes the complex easier to oxidize. The presence of relaxation in the ferrous chloride system thus lowers the ionization energy of the $2e\downarrow$ from that expected from the ground-state electronic structure. In addition, electronic relaxation changes the spatial distribution of the levels, the antibonding highest occupied level of the final state becoming delocalized over a ligand-based molecular orbital. Our previous study on cupric chloride also showed a large relaxation occuring on ionization, similar to that in the ferrous chloride complex. The large change in electron repulsion in this system also inverts the bonding scheme in the final Cu(III) state (producing a ligand-centered oxidation) and reduces the lowest energy ionization. Alternatively, only very limited relaxation effects are present in the Cu(I)/Cu(II) chloride redox couple. Both cuprous and cupric systems have normal ground-state-bonding schemes, with just a moderate increase in covalent mixing for cupric (65% Cu 3d averaged over the d band) relative to cuprous (85% Cu 3d) chloride due to the change in metal-centered electron repulsion.[4] Ferric chloride is also relatively unaffected by electronic relaxation; however, for this complex, both the initial- and final-state-bonding descriptions are inverted. Thus, in both cuprous and ferric chloride, the electronic relaxation is small and should not greatly affect redox processes. Variable-energy PES has now been shown to be a direct method for quantitatively determining electronic relaxation on ionization of transition-metal complexes that is large for specific metal ion oxidations and small for others. The contributions of electronic relaxation to redox processes of inorganic complexes in solution can now be quantitatively evaluated and will be a focus of future study.

Acknowledgment. We acknowledge the Stanford Synchrotron Radiation Laboratory (SSRL), which is supported by the U.S. Department of Energy, for providing beam time, the Stanford Center for Materials Research, which is supported by the Division of Materials Research of the National Science Foundation, for providing experimental facilities, and the National Science Foundation, Grant No. CHE-8613376, for financial support of this research. We thank M. Nerozzi for help in the crystal growing process and Jeff Guckert for assistance in the preparation of the manuscript.